



Spatial coherence of trajectory-resolved higher-order harmonics generated from an argon-filled gas cell using single- and two-color laser pulses

M. Kumar ^{1,2,*}, H. Singhal,^{1,2} A. Ansari ² and J. A. Chakera^{1,2}

¹Homi Bhabha National Institute, Anushakti Nagar, Mumbai 400094, India

²Laser Plasma Division, Raja Ramanna Centre for Advanced Technology, Indore 452013, India



(Received 12 June 2020; accepted 3 September 2020; published 1 October 2020)

An experimental study on spatial coherence of electron trajectory-resolved higher-order harmonic generation (HHG) in an argon-filled gas cell (length ~ 15 mm) using single-color ($\lambda \sim 800$ nm) and two-color laser pulses ($\lambda \sim 800$ nm + 400 nm) is performed. The contribution of both a long and short electron trajectory is observed in HHG using single-color laser pulse, whereas a dominant contribution of short trajectory is observed in HHG using two-color laser pulses. The spatial coherence of trajectory-resolved higher-order harmonics is investigated using a double slit experiment. The fringe visibility is higher (~ 0.7) at low gas cell pressure, for both short and long trajectory harmonics. At higher gas pressure (≥ 50 mbar), the fringe visibility of short trajectory harmonics (~ 0.7) is significantly higher than the long trajectory harmonics (~ 0.3 – 0.4). In the case of two-color laser pulses, the fringe visibility (~ 0.75) is found to be further higher than the single-color short trajectory harmonics and is nearly independent of gas pressure (~ 10 – 100 mbar). A theoretical model is used to explain the observed result and the intensity dependent dipole coefficient for short and long trajectory is estimated, which is in good agreement with the other reported results. The study provides an easy tool to study and control the role of different electron trajectories responsible for higher-order harmonic generation and also the spatial coherence property of higher-order harmonics generated from gas cell.

DOI: [10.1103/PhysRevA.102.043101](https://doi.org/10.1103/PhysRevA.102.043101)

I. INTRODUCTION

Higher-order harmonic generation (HHG) via an interaction of ultrashort intense laser pulse with underdense gaseous medium is a well-recognized technique for the generation of attosecond extreme ultraviolet pulses. The HHG using few cycle laser pulses has led to generation of isolated attosecond pulse, whereas the use of multicycle laser pulse has led to generation of attosecond pulse trains [1,2]. The phase locking between the higher-order harmonics remains a prerequisite for the generation of ultrashort attosecond pulses. There are several key factors which play a decisive role in generation of phase locked harmonics and have been addressed by several research groups [3,4]. In order to understand these factors, it is desirable to discuss briefly the mechanism of HHG. The generation of higher-order harmonics from the underdense gases was explained using the “three step model” proposed by Corkum *et al.* [5], which convincingly explained the whole process of HHG in three simple steps. In the first step, the presence of intense laser field distorts the Coulomb potential of atom, which leads to tunneling of the outermost bound electron of an atom. Subsequently, these tunneled electrons accelerate in the intense laser field and gains energy. With the reversal of the laser cycle, the electrons recollide back to the parent atom and recombine to give a high-energy photon. The acceleration of an electron in a laser field, which is

the second step of the three step model, is found to affect the spectral characteristics, divergence, as well as temporal characteristics of the generated harmonics [6,7]. It is therefore essential to understand and precisely control the electron motion in the laser field, to achieve short duration, coherent, and low divergence harmonics. It is found that the energy gained by the tunneled electron depends on the laser phase at which it is tunneled out from the atom [8]. Also, the electron tunneled at different laser phases undergoes different trajectories before it is recombined with the parent atom, which can be broadly classified into two categories: the short trajectory and the long trajectory [9]. The higher-order harmonic generated using these two trajectories have different time history and thus leads to different harmonic phase, known as the intensity dependent phase (IDP). The IDP is proportional to the intensity of the harmonic generating laser beam [10]. The constant of proportionality, known as the coefficient of IDP (α), varies with the nature of electron trajectory involved in the HHG process. The IDP coefficient of long trajectory (~ 20 to 25×10^{-14} cm²/W) is more than an order of magnitude higher than the short trajectory (~ 1 to 5×10^{-14} cm²/W) for the plateau harmonics [11]. The nature of the electron trajectory plays a crucial role in the spectral and divergence characteristics of the produced harmonics [7].

A few techniques have been proposed and also demonstrated to identify and control the electron trajectories. These techniques include the use of shaped laser beam [12], the use of two-color laser fields [13,14], optimization of focal position [15], etc. Also, the contribution of both short and long

*Author to whom correspondence should be addressed: mukund@rrcat.gov.in

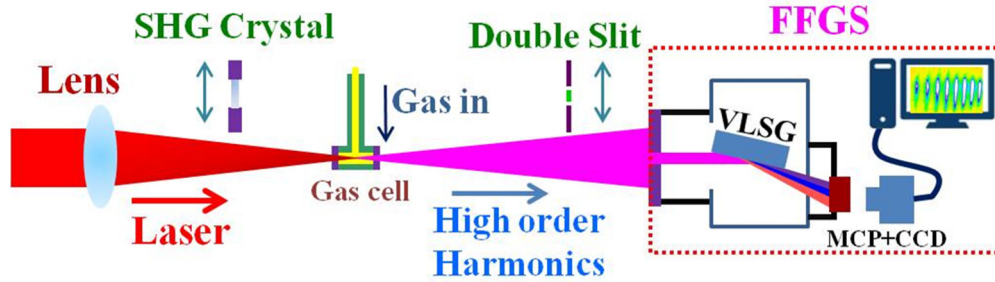


FIG. 1. A schematic diagram of the experimental setup used for higher-order harmonic generation from inert gas filled cell. The FFGS is flat field grating spectrograph, VLSG is variable line spaced grating, MCP is microchannel plate, and CCD is charge coupled device. A SHG crystal (BBO, thickness $\sim 100 \mu\text{m}$) is used for generating the two-color laser pulse, which comprises second-harmonic beam ($\lambda \sim 400 \text{ nm}$) as well as unconverted fundamental laser beam ($\lambda \sim 800 \text{ nm}$).

trajectory in HHG is observed, when the nonlinear medium is placed before the laser focus [15]. In this situation, the short trajectory is phase matched on the axis and the long trajectory is phase matched at off-axis positions. The relative contribution of these trajectories in HHG had also been estimated by several groups [16,17]. However, the spatial coherence property of harmonic generated by these trajectories is hitherto unexplored. The study of spatial coherence of the trajectory-resolved harmonics will add further insight into generation of coherent and ultrashort intense higher-order harmonic pulse. The study will also be helpful to control the coherence characteristics of attosecond harmonics, which is imperative for its application in ultrashort attosecond pump-probe studies [18], in ultrafast imaging [19], etc.

In this paper, we report an experimental study on spatial coherence of electron trajectory-resolved higher-order harmonics generated from an argon-filled cell in the pressure range from 10 to 100 mbar using single-color ($\lambda \sim 800 \text{ nm}$) and two-color laser pulses ($\lambda \sim 800 \text{ nm} + 400 \text{ nm}$). The electron trajectory-resolved harmonics can be generated by optimizing the laser and gas cell parameters, such as laser intensity, position of the gas cell relative to laser focus, and the gas cell pressure. It is found that under optimum parameter conditions of efficient harmonic generation using single-color laser pulse, there is a contribution from both short and long electron trajectories, whereas short trajectory is dominant in case of two-color laser pulses. Further, in the case of single color, increase in the spectral width of harmonics is observed at gas cell pressure $\geq 30 \text{ mbar}$ and the splitting in the spectrum is observed at gas pressure $\geq 60 \text{ mbar}$. For the two-color laser pulse generated harmonics, no significant change in the spectrum is observed. Next, study of spatial coherence shows that, for the single-color laser pulse, both short and long trajectory harmonics have high spatial coherence at low gas pressure ($\leq 30 \text{ mbar}$), whereas at high pressure the spatial coherence of short trajectory harmonics is significantly higher than the long trajectory harmonics. For the two-color laser pulse generated harmonics, the spatial coherence of harmonics is further higher than single-color short trajectory harmonics. The study clearly demonstrates different spatial coherent property of the harmonics generated from two trajectories and its control using two-color laser pulses.

II. EXPERIMENTAL SETUP

The experiment is performed using a chirped-pulse amplification-based Ti:sapphire kHz laser system, which provides a maximum energy of 7 mJ per pulse, at a laser pulse of $\sim 45 \text{ fs}$ [full width at half maximum (FWHM)] duration at central wavelength (λ_L) 800 nm. A schematic of the experimental setup is shown in Fig. 1. The laser pulse is focused in a gas cell of length $\sim 15 \text{ mm}$ and inner diameter $\sim 5 \text{ mm}$, using a planoconvex lens of focal length 750 mm ($f35$). The gas cell is sealed with 1 mm aluminum cover plates, placed at both sides of gas cell, i.e., at the entry and exit end of the gas cell. The focused laser pulse drills holes in these plates and paves the way for the collinearly propagating higher-order harmonics through the exit cover plate. The laser intensity is a crucial parameter in higher-order harmonic generation. For the measurement of laser intensity, it is important to experimentally measure the laser focal spot size. The measured focal spot is found to be elliptical, with beam diameter ($1/e^2$) of $\sim 70 \mu\text{m}$ in the horizontal direction and $\sim 45 \mu\text{m}$ in the vertical direction. The equivalent circular spot diameter is calculated to be $\sim 55 \mu\text{m}$ ($\sqrt{70 \times 45}$). The Rayleigh range for the Gaussian beam is calculated to be $\sim 3 \text{ mm}$. The laser energy of $\sim 5.5 \text{ mJ}$ is focused in the gas cell. The corresponding peak laser intensity is calculated to be $\sim 1 \times 10^{16} \text{ W/cm}^2$ at the laser focus ($z \approx 0$). The laser intensity can be varied by changing the position of the lens with respect to the gas cell to maximize the intensity of harmonic generated in the argon-filled gas cell at a particular gas pressure. The gas pressure inside the cell is monitored using a diaphragm gauge (make: Endress Hauser) installed with the gas flow line, which can measure the gas pressure from 1 mbar to 1 bar independent of gas type. Higher harmonics from the argon-filled cell are then dispersed and detected using an in-house developed flat field grating spectrograph (FFGS). The spectrograph consists of a variable line spaced (VLS) concave grating, which disperses as well as focuses wavelengths in a flat plane. The spectrum is detected on a microchannel plate (MCP) with a phosphor screen coupled to a charge-coupled device (CCD) camera. The grating has a central groove density of 1200 lines/mm. A ray tracing code is used for the precise wavelength dispersion and plate factor calibration of FFGS, by taking the grating parameter provided by the manufacturer [20] and the geometry used in

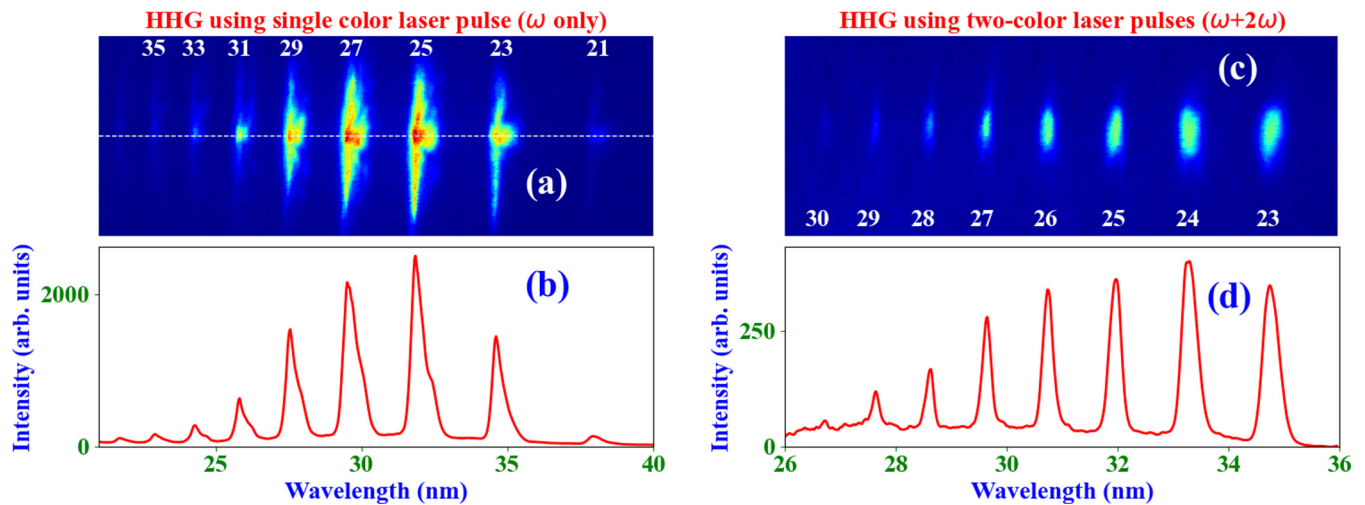


FIG. 2. The intensity of higher-order harmonics generated from argon filled cell using (a) single-color laser pulse; panel (b) shows line profile of (a), (c) using two-color laser pulses, and (d) shows the line profile of (c). The higher-order harmonic up to 35th order is observed in case of single-color laser pulse and up to 30th order in case of two-color laser pulses. The central region (laser propagation axis) is marked by a dashed line in (a).

the spectrograph. Standard wavelength at aluminum (Al) L edge ($\lambda \sim 17.1$ nm), is used to calibrate the FFGS dispersion in terms of wavelength with pixels. From the measured pixel position of Al L -edge, the FFGS is calibrated in the desired spectral range. The detail of FFGS calibration is reported in our published work [21].

To investigate the HHG using two-color laser pulse, the fundamental laser pulse ($\lambda \sim 800$ nm) and orthogonally polarized second-harmonic radiation ($\lambda \sim 400$ nm) is used. The two-color pulse is generated using a second-harmonic crystal [beta barium borate (BBO) crystal; thickness: 100 μm], placed in the path of a Ti:sapphire laser beam after the focusing lens. The crystal is placed at a safe distance away from the laser focus, so as to avoid damage of the crystal. The intensity of the laser pulse at the BBO crystal is $\sim 2 \times 10^{11}$ W/cm² (\sim an order of magnitude smaller than the damage threshold [22] of BBO). At this intensity of fundamental laser beam, the second-harmonic conversion efficiency is measured to be $\sim 10\%$. For the study of spatial coherence, a double slit (width ≈ 30 μm and separation ≈ 100 μm) is inserted in the path of higher-order harmonic radiation and the interference fringes of the dispersed harmonics is recorded using FFGS.

III. RESULTS

In order to generate the electron trajectory-resolved higher-order harmonics, the laser and gas cell parameters are optimized. The optimum gas cell position for maximum harmonic intensity is found to be ~ 15 mm before the laser focus, where the laser intensity is calculated to be $\sim 2.5 \times 10^{14}$ W/cm². The contribution from both short and long electron trajectory in the harmonic generation is observed in this condition. Figure 2 shows the harmonic spectrum generated at the above condition using single- and two-color laser fields. Figures 2(a) and 2(b) show the image and line profile of higher-order harmonics generated using a single-color laser pulse, where odd harmonic orders up to the 35th order have been observed. It can be seen from Fig. 2(a) that the har-

monic spectrum is significantly different in the on-axis region [marked with a dashed line in Fig. 2(a)] and the off-axis region. The spectral width is significantly higher in on-axis region as compared to the off-axis region. Figures 2(c) and 2(d) show the image and line profile of higher-order harmonics generated using two-color laser pulses ($\lambda \sim 800$ nm + 400 nm), where both odd and even harmonic orders with a harmonic cutoff up to the 30th order is observed. It is important to note that, in this case, the spectral features of harmonics are significantly different from the single-color generated harmonics. Here one can notice two different categories of higher-order harmonics. The on-axis harmonics (marked with dashed line) have small divergence, whereas the off-axis harmonics have significantly higher divergence and they are slightly shifted in wavelength also. Such spectral behavior is not observed in the HHG spectrum recorded using two-color laser pulses.

Several groups have reported the broadening and splitting in the harmonic spectrum with increase in laser intensity [16,23], however there are only a few studies reported on the effect of gas cell pressure in the higher-order harmonic spectrum [24]. It is found that the broadening and splitting in the harmonic spectrum is mainly due to the contribution of short and long electron trajectories responsible for HHG. We have carried out a study on the spectral features of harmonics with gas cell pressure. For this, the harmonic intensity is maximized first by varying the gas cell position relative to laser focus and then gas pressure inside cell was varied. Figure 3(a) shows the variation of the harmonic spectrum at different gas cell pressures generated using single-color laser pulse and only odd orders in the harmonic spectrum are seen. The intensity plot of the harmonic spectrum at different gas cell pressures is shown in Fig. 3(b). The expected position of harmonic orders is marked by a dashed line in Figs. 3(a) and 3(b), for the driving laser wavelength of ~ 800 nm. It may be seen that the harmonic spectral width is smaller at lower gas pressure and it increases with increase in gas pressure and it shows splitting at higher pressure. For example, the width of

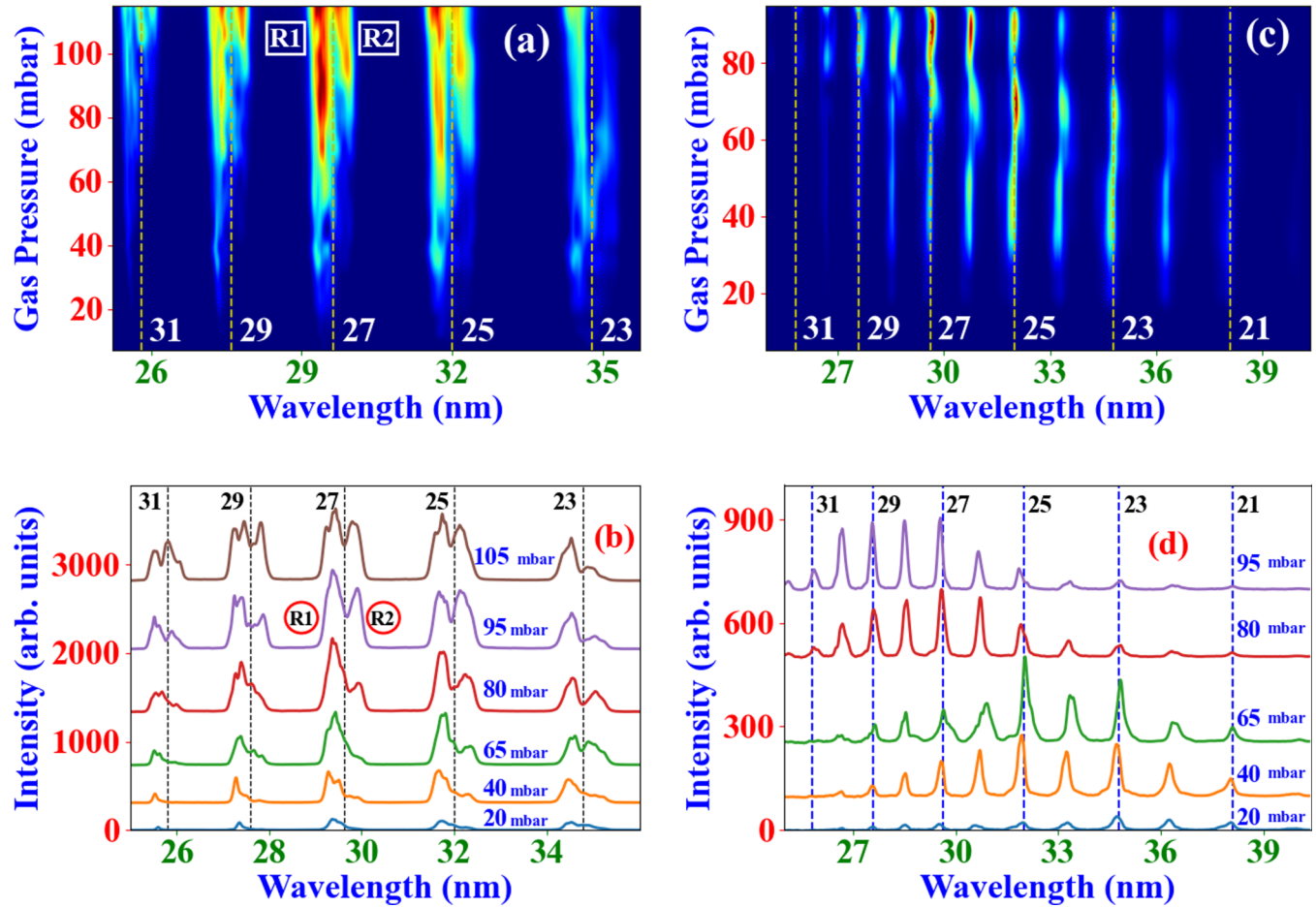


FIG. 3. The figure shows variation of harmonic intensity and spectrum with gas cell pressure using (a) single-color laser pulse; panel (b) is line profile of (a) at 20, 40, 65, 80, 95, and 105 mbar. Panel (c) shows the variation for the two-color case and (d) is line profile of (c) at 20, 40, 65, 80, and 95 mbar. The splitting in harmonic spectrum at higher gas pressure (≥ 40 mbar) is clearly seen in (a), which is absent in (c). It can be seen in figure that the harmonic spectrum changes with increase in gas pressure and at high gas pressure (> 60 mbar) there is splitting in the spectrum. The wavelength position of harmonic orders is shown by dashed lined in (a)–(d). The spectral region on the blue side of dashed line is represented as region R1 and the region on the red side of dashed line is marked as R2.

the 27th harmonic order is ~ 0.35 nm (FWHM) at 20 mbar gas pressure, and it increases to 0.45 nm at ~ 55 mbar pressure. The splitting in the harmonic order is observed at gas pressure ≥ 60 mbar, which is marked as R1 and R2 in Figs. 3(a) and 3(b). The blueshifted harmonic spectrum is marked as region R1 and the redshifted is marked as R2. Figure 3(c) shows the variation of harmonic spectrum with gas pressure in the case of two-color laser pulses. Here one can see both odd as well as even harmonics. Figure 3(d) shows the intensity line profile of harmonics taken at different gas pressures. It can be seen from Figs. 3(c) and 3(d) that there is hardly any splitting or spectral shift with the gas pressure. It is therefore evident from above results that there is a significant change in the spectral characteristics of harmonics in the case of single-color laser generated harmonics and it remains unchanged for the two-color case.

To investigate the role of electron trajectories in HHG further, we have carried out the study of spatial coherence of higher-order harmonics under different gas pressures using both single- and two-color laser pulses. A double slit is placed before FFGS as shown in Fig. 1. The slit (width $\approx 30 \mu\text{m}$ and separation $\approx 100 \mu\text{m}$) was placed at ~ 500

mm from the center of the gas cell. The distance between the slit and the MCP detector of FFGS was ~ 825 mm. Figure 4 shows interference fringes recorded using a double slit at ~ 40 mbar gas pressure for the 23rd harmonic generated from both single- and two-color laser pulses. The fringes for the shifted or splitted harmonic spectra could also be recorded quite clearly in the case of single-color generated harmonic spectra as shown in Fig. 4(a). The splitted components are marked for 23rd-harmonic order as R1 and R2 [Fig. 4(a)]. Similar fringes were also recorded for higher-order harmonics in the case of the two-color laser pulse. The line profile of interference fringes in two regions of the splitted component in the single-color case and for the two-color case for the 23rd-harmonic order is plotted in Fig. 4(b). Fringe visibility $[(V) = (I_{\text{max}} - I_{\text{min}})/(I_{\text{max}} + I_{\text{min}})]$ is calculated from the maxima and minima of the intensity of interference fringes. It is calculated to be ~ 0.72 for two-color harmonics, and 0.63 and ~ 0.48 for the harmonics in regions R1 and R2 respectively.

Next, the spatial coherence property of the higher-order harmonics from the 23rd to 31st orders in the gas pressure ranging from ~ 10 to ~ 120 mbar is investigated. Figure 5

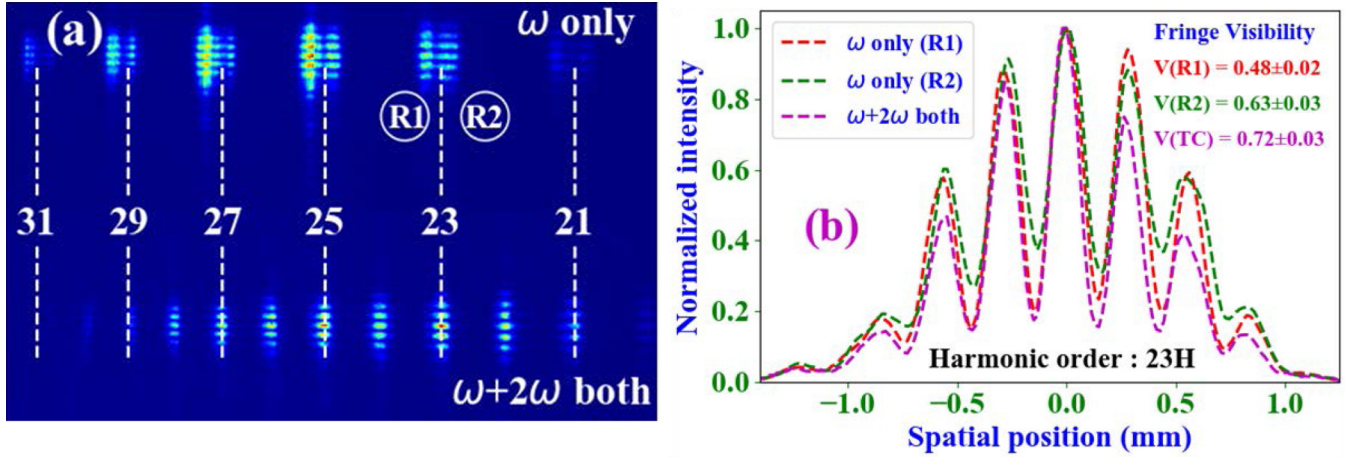


FIG. 4. Panel (a) shows the image of interference fringes of harmonics generated using single- and two-color laser pulses. The two splitted regions in the interference fringe of HHG generated using single-color case are marked as R1 and R2. Panel (b) shows the line profile of interference pattern and the measured fringe visibility of 23rd-harmonic orders for single-color (region R1 and R2) and two-color case. The fringe visibility of harmonics generated using two-color case is higher than single-color case and also the visibility of HHG in region R2 is higher than that of region R1.

shows the measured fringe visibility for the harmonic 23rd (lower), 27th (mid), and 31st (cutoff harmonic) orders generated using single-color (regions R1 and R2) and two-color laser pulses at different gas pressures. The fringe visibility for the two-color case is always higher than that of the single-color beam in the complete gas pressure range and it remains nearly constant in the gas pressure range of our study. For the harmonics generated using single-color laser pulse, the fringe visibility of region R2 is higher than that of region R1 (smaller than the two-color case). In region R1, the fringe visibility decreases with an increase in gas pressure (see Fig. 5),

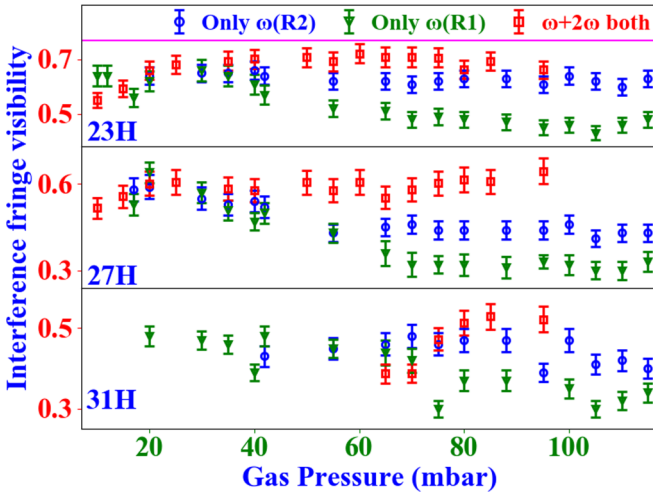


FIG. 5. The figure shows the variation of interference fringe visibility for three harmonic orders 23rd, 27th, and 31st order. The visibility for all harmonic orders in whole gas pressure range is higher for two-color case. In case of HHG using single-color laser pulse, the fringe visibility is higher for HHG in spectral region R2, as compared to spectral region R1. At small gas pressure (<30 mbar), the fringe visibility of HHG in both spectral regions (R1 and R2) is similar, whereas at gas pressure >30 mbar the visibility of harmonics in region R1 decreases with increase in gas pressure, and at higher gas pressure (>70 mbar) it remains constant.

whereas in region R2 it remains nearly the same in the whole pressure range (10–120 mbar) and it is valid for all harmonic orders. Further, the fringe visibility is found to decrease with an increase in harmonic orders for both single- and two-color cases.

IV. DISCUSSION AND ANALYSIS OF THE OBSERVED RESULTS

The study by Auguste *et al.* [15] has shown that by focusing the laser pulse after the gas cell, the generated harmonics has a contribution from both the long and short trajectories. In this condition, there is better phase matching for both short and long trajectory harmonics. The short trajectory harmonics are phase matched on axis, whereas the long trajectory harmonics are phase matched off axis [15]. In the present study, we have focused the laser pulse after the gas cell (~ 15 mm), where intense harmonic generation is observed in our case. The recorded harmonic spectrum using FFGS [see Fig. 2(a)] shows that there is a contribution from short as well as long electron trajectories, which is identified from their different divergences and spectral widths.

A. Influence of electron trajectories in harmonic spectrum and divergence

The spectral characteristics of the higher-order harmonics generated from an underdense gas medium has a contribution from several factors, e.g., the increase in spectral width of laser pulse due to self-phase modulation, due to intensity dependent dipole phase (IDP), etc. [23,25]. The instantaneous frequency of the q th-harmonic order can be expressed as

$$\omega_q(t) = q\omega_L + \Delta\omega_{q,SPM}(t) + \Delta\omega_{q,IDP}(t),$$

$$\text{where } \Delta\omega_{q,SPM}(t) = -\frac{2\pi q}{\lambda_L} \int_0^{L_{med}} \frac{\partial n(t)}{\partial t} dz$$

$$\text{and } \Delta\omega_{q,IDP}(t) = \alpha_q^i \frac{\partial I}{\partial t}. \quad (1)$$

$n(t)$ is the refractive index due to the free electron and the neutral atom present in the medium, α_q^i is the dipole phase coefficient for the q th-harmonic order (the superscript i corresponds to the i th electron trajectory, $i = 1$ is for the short trajectory, and $i = 2$ is for the long trajectory) [11,26]. Equation (1) has three terms: the first term corresponds to the frequency of the q th harmonic at the central laser frequency (ω_L), the second term corresponds to the contribution of the additional frequency generated due to self-phase modulation (SPM) of the laser pulse, and the third term corresponds to the additional frequency generated due to the time-dependent IDP. In order to estimate the contribution of the second term in Eq. (1), the spectrum of the fundamental laser pulse is measured (at 120 mbar gas cell pressure), before and after the gas cell. The laser spectral width ($\Delta\lambda$) at full width at half maximum (FWHM) value is measured to be ~ 22.1 , 24, and 27 nm before the focusing lens, after the focusing lens, and after the focused laser beam propagation through the gas cell, respectively. Thus, the increase in the spectral width of the laser pulse in the gas cell is ~ 3 nm, at a gas pressure of 120 mbar. The second term in Eq. (1) can be calculated to be $\Delta\omega_{q,SPM} = q\Delta\omega_{L,SPM} = q\omega_L(\Delta\lambda_L/\lambda_L)$ for the q th-harmonic order. For example for the 27th-harmonic order, the change in spectral width due to second term of Eq. (1) is calculated to be ~ 0.1 nm, which is much smaller than the overall spectral width of the 27th-harmonic order (~ 0.9 nm) as measured experimentally [see Fig. 3(b)]. Therefore the third term (IDP) of Eq. (1) has a significant contribution in the observed increase in the spectral width of the harmonics. It may be noted from Eq. (1) that the spectral width depends on the type of electron trajectories contributing for HHG. This can be significantly different for long and short trajectories [24,27]. As the α_L (for long trajectory) is significantly higher than α_S (for short trajectory) [10,24], the harmonic generated from the short trajectory will have small spectral width or spectral shift as compared to the harmonics generated from long trajectory and the same is also observed experimentally (Fig. 3).

The divergence of higher-order harmonics generated from different trajectories may also be significantly different [23,24]. Normally, it is observed that the harmonics have a Gaussian spatial profile and therefore the radial phase can be given by the following expression for various electron trajectories [25]:

$$\begin{aligned}\phi_q(r) &\approx -\alpha_q^i I(r) \approx -\alpha_q^i I_0 \exp\left(-\frac{2r^2}{w_0^2}\right) \\ &\approx -\alpha_q^i I_0 \left(1 - \frac{2r^2}{w_0^2}\right) \quad (\text{for } r \ll w_0),\end{aligned}\quad (2)$$

where w_0 is the $1/e^2$ laser beam waist radius and r is the radial coordinate from the axis. The radial phase $[\phi(r)]$ of the harmonics for the different trajectories will be significantly different (as $\alpha_L \gg \alpha_S$). It is higher by an order of magnitude in the case of long trajectories compared to shorter trajectories [11,26]. Due to a large difference in the radial phase, the generated harmonics from the two trajectories have significantly different divergences [12]. The difference in divergence and spectral width is therefore a key parameter to identify the long and short trajectory contributions in harmonic spectra from its far-field profile [24]. In our present experimental observations

(Figs. 2 and 3) it is clearly seen that the harmonic spectra show different divergence as well as spectral width. Thus, there is clear evidence of contributions from both short as well as long electron trajectories. The harmonics generated with low divergence [close to dashed line in Fig. 2(a)] can be attributed to short trajectory and the higher divergence to the long trajectory.

The spectral shift or splitting of the harmonic spectrum [Figs. 3(a) and 3(b)] can be explained by considering the effect of a time-dependent phase imparted by IDP (due to time varying laser intensity). The instantaneous frequency of the generated harmonics can be expressed as the sum of the first and third terms of Eq. (1). The third term (IDP contribution) depends on the rate of change of laser intensity with time. If the rate is positive ($dI/dt > 0$), there would be a blueshift, and a negative rate ($dI/dt < 0$) leads to a redshift of the harmonic spectrum [17]. The trajectory-resolved phase matching simulation has shown that, for the long trajectory, phase matching is better on the leading edge of a laser pulse, whereas for the short trajectory, the phase matching is better on the trailing edge [17]. Further, a detailed study on the spectral characteristics of higher-order harmonics performed by Nefedova *et al.* [6] have shown that the blueshift or redshift in the harmonic spectrum generated in argon gas (25th order) due to the particular trajectory depends on the laser intensity relative to the phase matching intensity (I_{PM}), viz., the intensity where the contribution due to free electron and atomic dispersion in the nonlinear medium balance each other. They have also found that at low laser intensity ($I < I_{PM}$, phase matching intensity), the short trajectory leads to blueshift and the long trajectory leads to redshift. At higher laser intensity, ($I > I_{PM}$), the short trajectory harmonics are redshifted, whereas the long trajectory harmonics are blueshifted. In order to estimate phase matching intensity, the phase matching fractional ionization level is needed to be calculated. In the present study, for 23rd harmonic order, the fractional ionization is calculated to be ~ 0.2 , and the phase matching intensity is calculated using ADK theory to be 1.5×10^{14} W/cm². However, the laser intensity used in the present study was $\sim 2.5 \times 10^{14}$ W/cm², which is significantly higher than the above estimated phase matching intensity. Therefore the harmonic generated using the short trajectory is expected to be redshifted, whereas the harmonic generated using the long trajectory should be blueshifted, which is in line with our experimental observations.

B. Effect of gas pressure in the harmonic spectrum: Single color vs two color

We will now discuss the effect of gas pressure on trajectory contributions and expected harmonic spectrum characteristics. Let us explore how laser intensity is affected by a change in the gas pressure of a gas cell. At laser intensity $\sim 2.5 \times 10^{14}$ W/cm², the underdense Ar gas in the cell is significantly ionized. The ionization rate is estimated using the ADK formulism [28]. The spatiotemporal profile of the laser pulse, focused in the gas cell, gives rise to spatiotemporal variation in the free-electron density in the medium. This density variation may lead to a reduction in laser intensity due to processes like ionization induced defocusing (density for

significant defocusing effect is given as $n_e \approx \lambda N_c / 2z_R$, for an 800-nm wavelength and it is calculated to be $\sim 2 \times 10^{15} \text{ cm}^{-3}$ [29]) of the laser beam. The defocusing effect will be more prominent as the gas pressure inside the cell increases and the laser intensity may reduce sharply at higher gas pressure. This reduction in the laser intensity may result in generation of higher-order harmonics on both sides (leading and trailing edge) of the laser pulse. Further, the temporal change in the laser intensity (dI/dt) due to a change in the gas pressure will lead to a different spectral shift in the harmonic spectrum (due to long and short trajectory contribution). This effect can be clearly seen in the experimental results (Fig. 3).

It is important to note here that the selection of an electron trajectory using two-color laser pulses depends on the ratio of the fundamental and second-harmonic laser fields and their relative phase. The theoretical study by Kim *et al.* [14] has shown that in the case of orthogonally polarized two-color pulses, the trajectory selection is nearly independent of the ratio of the magnitude of fundamental and second-harmonic fields. The short trajectory is preferably selected when the relative phase between the two is $\sim \pi/2$. It is extremely challenging to experimentally measure and tune the relative phase between the two colors precisely, particularly for a multicycle fundamental laser pulse. In the present setup, we didn't have a provision to measure and tune the relative phase between the two frequencies ($\lambda \sim 800 \text{ nm}$ and $\lambda \sim 400 \text{ nm}$). However, the identification of the long and short trajectory is confirmed from the measured divergence spectrum as well as the difference in spatial coherence of the harmonics generated by the two trajectories. The selection of the short trajectory using two-color pulses in our case shows that the relative phase between the fundamental and two colors may be close to $\pi/2$ [14]. In the observed harmonic spectrum [Fig. 2(b)], it is evident that the most contribution in the harmonic spectrum is from short trajectory electrons as the harmonic beam divergence is low. Now the question remains as to why there is no significant spectral shift with a change in the gas pressure. This may be attributed to the low intensity of two-color laser pulses during interaction in the gas cell. The dominant factors responsible for the low intensity are the low second-harmonic conversion in the BBO crystal ($\sim 10\%$) and the "B" integral distortion in the beam after the transmission from the crystal [30]. The laser intensity becomes $\sim 5 \times 10^{13} \text{ W/cm}^2$ for the second-harmonic beam. Due to this, the effect of ionization induced defocusing will be substantially reduced and hence no change in the harmonic spectrum with change in gas pressure is observed. Further, the low laser intensity may also lead to the generation of harmonics in both the leading and trailing edge of the laser pulse. However, the magnitude of the IDP term in Eq. (1) (the $\alpha \times dI/dt$ term) will be also small in this case and hence no significant redshift or blueshift would be observed.

C. Spatial coherence of long and short trajectory harmonics: Theory

We now discuss the spatial coherence characteristics of the trajectory-resolved harmonics. A few studies have shown that the temporal coherence properties of the harmonics generated from these two trajectories are different [11], i.e., the

higher-order harmonic generated from the short trajectory have a higher temporal coherence [11]. However, the spatial coherence property of the spectrally resolved harmonics in particular is not reported and remains unexplored. High spatial coherence of the harmonic source is quite desirable for various applications and has already been demonstrated in various research fields, viz., lensless imaging [19,31], holography [32], lithography [33], and time-resolved high-density plasma probing [34], etc. For all these applications high spatial coherence is essential and preferably throughout the spectrum of harmonics used for such applications. As described earlier, the spatial coherence of higher-order harmonics varies across the spectrum of each individual harmonic order (Fig. 5), which makes the study interesting and also essential to understand the mechanisms responsible for such behavior. This will provide a tool to achieve high spatial coherence across the harmonic spectrum. Normally, the harmonic spectrum is supposed to have high and the same coherence across the full spectrum due to the coherent generation process. However, there are several factors which deteriorate its coherence property as discussed below.

For a source, the spatial coherence is expressed in terms of the correlation of the electric field between any two points on the source. It is quantitatively expressed in terms of the normalized complex degree of coherence (μ_{12}), which is equal to the experimentally measured fringe visibility [35]. Hence, the spatial coherence is affected by all the factors that impart the time-dependent phase, transverse to the beam propagation direction [36]. For the higher-order harmonic radiation source, there are two dominant factors, which may affect its spatial coherence. These are the time-dependent free-electron density in the medium and the intensity dependent dipole phase [36]. Ditmire *et al.* [36] estimated the fringe visibility theoretically, where the dominant contribution by the free-electron density fluctuation in the nonlinear medium is taken into account and the effect of IDP was neglected. In another study by Déroff *et al.* [37], the roles of both the free-electron density fluctuation and the IDP phase were taken into account to explain their observations. Most of these studies were performed in HHG from gas jets and not from the long length gas cell as reported here.

For most of the theoretical calculations of spatial coherence of higher-order harmonics, a point source is usually considered. However, practically it has finite size, which affects its spatial coherence, as multiple points on the source (due to its finite size) may create its double slit interference pattern, which leads to a reduction in fringe contrast [38]. Thus finite source size may significantly deteriorate the spatial coherence of a source [36].

We now try to understand the experimentally observed results based on the above discussions. Let us consider that the higher-order harmonics are generated at the center of the gas cell, in the laser propagation direction ($z = 0$). Due to significantly different divergence, the source size of long and short trajectory harmonics at the exit of the gas cell will also be different. The difference in source size (at the exit of the gas cell) will lead to a different maximum electron density fluctuation experienced by long and short trajectory generated harmonics. This will lead to different spatial coherence of harmonics generated from these electron trajectories.

Let us calculate the spatial coherence of the source by considering the two transverse points on the harmonics source. The calculation is performed by considering the free-electron density fluctuation in the gas cell, which may also lead to a fluctuation in the laser intensity. Considering the linear variation of free-electron density [36] and the laser intensity (assuming the harmonic source size is smaller than the laser focal spot size) at two transverse points, we have

$$n_e^i(t) = \begin{cases} (n_e + \delta n_e) \frac{t}{\tau_p} & \text{for } i = 1 \\ n_e \frac{t}{\tau_p} & \text{for } i = 2 \end{cases}$$

$$\text{and } I^i(t) = \begin{cases} (I + \delta I) \frac{t}{\tau_p} & \text{for } i = 1 \\ I \frac{t}{\tau_p} & \text{for } i = 2, \end{cases} \quad (3)$$

where n_e is the background electron density, $i(=1, 2)$ is indices referring to two points on the transverse dimension of the harmonic source, n_e^i is the electron density at the two points, and I^i is the laser intensity at the two sampled points, δn_e is the electron density fluctuation, I is the peak laser intensity, δI is the fluctuation in laser intensity at two points transverse to the harmonics propagation, and τ_p is the laser pulse duration. From Eq. (3), the time-dependent phase difference between the two points, by considering both the free-electron density fluctuation and the IDP phase (calculated for Gaussian beam profile [39]), can be expressed as

$$\Delta\phi(t) = \Delta k L_{\text{med}}/2 = \left(\frac{\pi q L_{\text{med}}}{2\lambda_L n_{\text{crit}}} \delta n_e - \frac{z z_R^2 \alpha_q L_{\text{med}}}{(z^2 + z_R^2)^2} \delta I_0 \right) \frac{t}{\tau_p}. \quad (4)$$

The complex degree of coherence (equal to the fringe visibility) is calculated from the time-averaged electric-field correlation between any two sampled points on the harmonic beam [36]. We have added the contribution of the IDP phase (considering the linear variation of the laser intensity at the two sampled points) to the fringe visibility expression given by Ditmire *et al.* [36]. The fringe visibility is evaluated using the following expression:

$$\text{Fringe visibility } (V) \approx \left| \text{sinc} \left[\frac{\pi q L_{\text{med}}}{4\lambda_L n_{\text{crit}}} \delta n_e - \frac{z z_R^2 \alpha_q L_{\text{med}}}{2(z^2 + z_R^2)^2} \delta I_0 \right] \right|, \quad (5)$$

where L_{med} is the length of the gas cell, δn_e is the electron density fluctuation of the two points, λ_L is the laser wavelength, n_{crit} is the critical density at wavelength λ_L , q is the harmonic order, z is the position of the gas cell relative to laser focus (~ -15 mm), Z_R is the Rayleigh range of the focused laser beam, δI is the laser intensity fluctuation between the two points, α_q is the IDP coefficient for the short and long trajectory for a given harmonic order. At the gas cell position ($z = -15$ mm), Rayleigh range ~ 3 mm, $n_{\text{crit}} \sim 1.7 \times 10^{21} \text{ cm}^{-3}$, $L_{\text{med}} \sim 15$ mm, the fringe visibility expression [Eq. (5)] simplifies to

$$V \approx |\text{sinc}\{8.65q[\delta n_e(10^{18} \text{ cm}^{-3}) + 0.02[\alpha_q(\text{cm}^2/\text{W})][\delta I_0(\text{W}/\text{cm}^2)]]\}|. \quad (6)$$

It can be seen in Eq. (6), that the fringe visibility depends on the fluctuations in the free-electron density and the laser

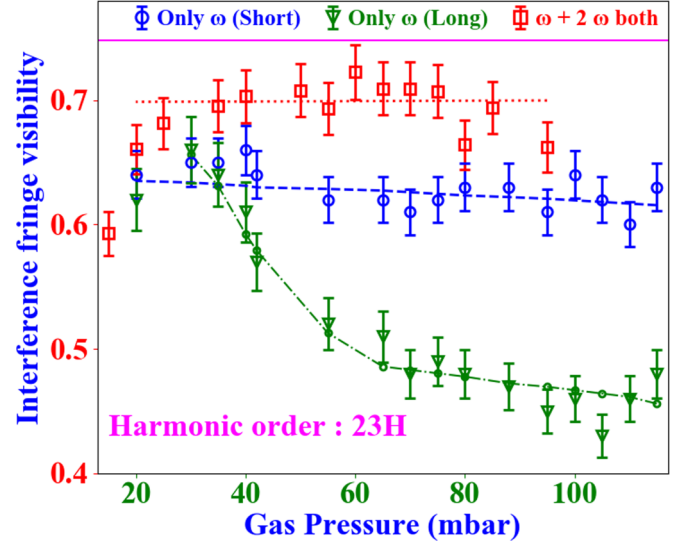


FIG. 6. The experimentally measured fringe visibility (scattered points) and calculated fringe visibility for 23rd-harmonic order with increase in gas pressure from ~ 15 to ~ 120 mbar. The square, circle, and triangle symbols represent the experimental visibility and the dotted, dashed, dash-dotted lines represent the theoretical fitting for two-color harmonics, short trajectory, and long trajectory harmonics respectively. The theoretically calculated fringe visibility matched fairly well with the experimentally measured fringe visibility.

intensity across the harmonic source size (at the exit of the gas cell), on harmonic order, and on the IDP coefficient.

D. Effect of gas pressure on spatial coherence of long and short trajectory harmonics

From the above discussion it is evident that the laser intensity and free-electron density fluctuation across the harmonic source crucially affects its spatial coherence property. There are two major sources of these fluctuations. The first is the fluctuation in the atomic density in gas cell, arising due to the dynamics of gas flow through micron-size hole drilled by the laser pulse at the entry and exit of the gas cell, and the second is the variation in the laser intensity in the transverse direction to the laser propagation. With an increase in gas pressure, the background electron density increases, thus the density fluctuation is also expected to increase and will reduce the fringe visibility [Eq. (6)]. Now if we compare our experimental observations on fringe visibility with gas pressure (Fig. 6), it is observed that for the single-color short trajectory harmonics as well as for the two-color generated harmonics, the fringe visibility is nearly independent of gas pressure. For the long trajectory harmonics, with an increase in gas pressure, the fringe visibility first decreases (up to pressure ≤ 60 mbar) and then it becomes nearly constant with an increase in gas pressure (pressure ≥ 60 mbar). Such behavior can be understood by considering the dynamics of gas flow at the two orifices created in aluminium end caps (~ 1 mm thick) by the laser pulse at the exit end of the gas cell. In the gas pressure range of 10–100 mbar used in the current experiments, the mean free path of the argon atom in the gas cell is expected to be in the range of ~ 7 – 0.7 μm respectively

at room temperature. The dynamics of gas flow is expressed in terms of Knudsen number ($K_n = \lambda/L$, where λ is the mean free path and L is the characteristic length scale). The L is nothing but the orifice drilled by the laser pulse in the gas cell end caps. This was measured to be $\sim 80 \mu\text{m}$. Thus the Knudsen number is estimated to be ~ 0.1 – 0.01 at 10 and 100 mbar respectively. At higher Knudsen number (0.1) the gas flow is in the slip flow regime [40], where the gradient in gas density and the temperature gradient is present close to the orifice wall. This will lead to an increase in gas density fluctuation close to the orifice wall. On moving away from the orifice wall, i.e., close to the laser axis ($r = 0$), the gas density fluctuation is reduced. At higher gas pressure, the background gas density increases, which should increase the gas density fluctuation. However, the Knudsen number decreases (with increase in gas pressure), which makes the gas flow more continuous and reduces the density fluctuation. Due to these two counterprocesses, the density fluctuations at the orifice will remain almost constant beyond a certain gas pressure and result in similar spatial coherence beyond that pressure. In the present study, it was observed that at ~ 60 mbar gas pressure and above, the fringe visibility becomes constant (Fig. 5).

Next, the harmonic beam diameter at the exit of gas cell is calculated from the higher-order harmonic spectra recorded using FFGS, by considering the geometrical parameters of the harmonic beam propagation. It was calculated to be ~ 75 and $\sim 15 \mu\text{m}$ for the long and short trajectory respectively. It may be compared with the exit aperture of the gas cell, which is $\sim 80 \mu\text{m}$. Thus, the harmonics generated from the long and short trajectories will pass through the orifice without clipping. Further, the long trajectory harmonic beam size at the gas cell exit is similar to the diameter of the laser drilled orifice ($\sim 80 \mu\text{m}$); it experiences the higher density fluctuation compared to the short trajectory harmonics.

The experimentally observed fringe visibility for 23rd-harmonic order generated by short and long trajectories with single- and two-color laser pulse in the gas pressure range of 20–120 mbar is shown in Fig. 6. The experimentally observed fringe visibility can be fitted with the theoretically estimated one using Eq. (6) as described earlier. The background electron density in the plasma which generates efficient harmonics can be determined using relation $\Delta k \times L_{\text{med}} \sim 2\pi$ [36]. It is calculated to be ~ 2 – $3 \times 10^{16} \text{cm}^{-3}$. For fitting the experimentally measured fringe visibility for 23rd-harmonic order generated using single-color (long and short trajectory) and two-color laser pulses, the maximum free-electron density fluctuation (δne) is taken to be ~ 2.5 to $\sim 3 \times 10^{15} \text{cm}^{-3}$ for short trajectory harmonics in the whole pressure range (~ 10 to ~ 120 mbar), ~ 2.5 to $\sim 3 \times 10^{15} \text{cm}^{-3}$ for long trajectory harmonics in the gas pressure range of 20–60 mbar, $\sim 3 \times 10^{15} \text{cm}^{-3}$ in the gas pressure range from ~ 60 to ~ 120 mbar, and $\delta ne \sim 2 \times 10^{15} \text{cm}^{-3}$ for the two-color harmonics. The maximum free-electron density fluctuation taken for fitting the fringe visibility in Fig. 6 is $\sim 10\%$ of the background density, which is in line with our earlier observations [41]. The IDP coefficients of $\sim 23 \times 10^{-14} \text{cm}^2/\text{W}$ for the long, and $5 \times 10^{-14} \text{cm}^2/\text{W}$ for both short trajectory and two-color harmonics [42], fluctuation in laser intensity of $\sim 5\%$ of the peak value ($\sim 10^{13} \text{W}/\text{cm}^2$), the calculated

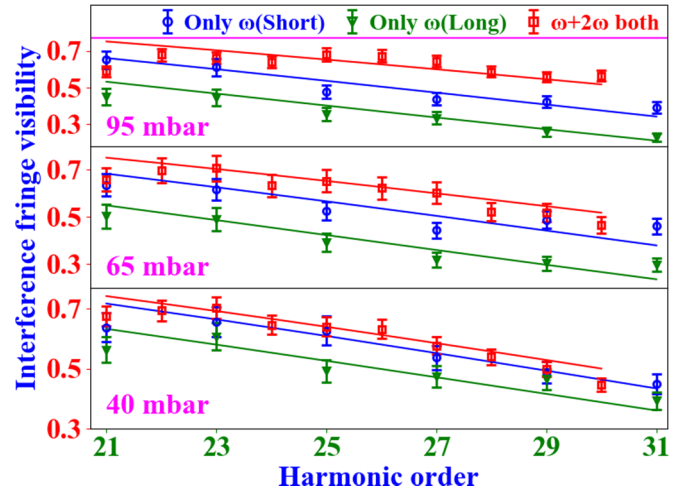


FIG. 7. The variation of experimentally measured and theoretically calculated fringe visibility with harmonic order at 40-, 65-, and 95-mbar pressure. The three gas cell pressures are in low-, intermediate-, and high-pressure regime. The calculated and measured value match well for all harmonic orders.

fringe visibility matches well with the experimentally observed fringe visibility for the 23rd-order harmonic order (see Fig. 6).

Considering the fluctuation in free-electron density and laser intensity estimated for the 23rd harmonic above, the fringe visibility is calculated for the 21st- to 31st-harmonic orders, in low (40 mbar), intermediate (65 mbar), and high gas pressure (95 mbar). Figure 7 shows the experimentally measured fringe visibility for the higher-order harmonic in the range of 21st to 31st odd orders at 40-, 65-, and 95-mbar gas pressure. It is found that the fringe visibility matches closely the IDP coefficients of $25 \times 10^{-14} \text{cm}^2/\text{W}$ (for 21st order), $23 \times 10^{-14} \text{cm}^2/\text{W}$ (for 23rd order), $20 \times 10^{-14} \text{cm}^2/\text{W}$ (for 25th order), $18 \times 10^{-14} \text{cm}^2/\text{W}$ (for 27th order), $15 \times 10^{-14} \text{cm}^2/\text{W}$ (for 29th order), and $13 \times 10^{-14} \text{cm}^2/\text{W}$ (for 31st order) for the long trajectory harmonics. Similarly for the short trajectory, it is found to be $5 \times 10^{-14} \text{cm}^2/\text{W}$, $7 \times 10^{-14} \text{cm}^2/\text{W}$, $8 \times 10^{-14} \text{cm}^2/\text{W}$, $10 \times 10^{-14} \text{cm}^2/\text{W}$, $12 \times 10^{-14} \text{cm}^2/\text{W}$, $13 \times 10^{-14} \text{cm}^2/\text{W}$ for 21st to 31st order respectively. For the two-color harmonics the IDP coefficient is taken to be the same as that of short trajectory harmonics. The above derived values of the IDP coefficient are in agreement with the earlier reported values [42]. The above discussion shows that the study of spatial coherence of spectrally resolved harmonics can be used to infer the contribution of different electron trajectories in higher-order harmonic generation.

V. CONCLUSIONS

In conclusion, the trajectory-resolved higher-order harmonics are generated in an argon-filled gas cell using single- and two-color laser fields. The long and short electron trajectory contributions are identified from the difference in the spectrum and divergence of harmonics, generated from these trajectories. The divergence of long trajectory harmonics is found to be more than five times higher than that of short

trajectory harmonics. The spectrum of long trajectory harmonics is blueshifted and the spectrum of short trajectory harmonics is redshifted. Further, the study of spatial coherence of electron trajectory-resolved harmonics shows that at high gas pressures (≥ 60 mbar), the spatial coherence of short trajectory harmonics is significantly higher compared to that of long trajectory harmonics. Due to the small source size at the gas cell exit compared to the laser drilled orifice, the short trajectory harmonics is not much influenced by the gas flow dynamics and shows high fringe visibility, which is nearly independent of gas pressure. The long trajectory harmonics are highly affected by the gas flow dynamics, due to the large source size at the gas cell exit, and show peculiar behavior in variation of fringe visibility with the gas pressure. The theoretical model is used to explain the experimental observations. From the theoretical fitting of experimentally measured fringe

visibility, the IDP coefficient is estimated, which matched well the earlier reported values. The study shows a different spatial coherent property of the harmonics generated from two trajectories, which is important to generate a coherent and intense higher-order harmonic source for various important applications.

ACKNOWLEDGMENTS

The authors would like to acknowledge R. P. Kushwaha, S. Sebastin, K. C. Parmar, and L. Kisku for mechanical support as well as their help in setting up the experiment, and R.A. Joshi and R. K. Bhat for their help in the laser operation. The authors would also like to acknowledge the laser electronic support division for providing electronic support during the experiment.

-
- [1] F. Calegari, G. Sansone, S. Stagira, C. Vozzi, and M. Nisoli, *J. Phys. B: At. Mol. Opt. Phys.* **49**, 062001 (2016).
- [2] F. Krausz, *Phys. Scr.* **91**, 063011 (2016).
- [3] P. Antoine, A. L'Huillier, and M. Lewenstein, *Phys. Rev. Lett.* **77**, 1234 (1996).
- [4] P. Agostini and L. F. DiMauro, *Rep. Prog. Phys.* **67**, 1563 (2004).
- [5] P. B. Corkum, *Phys. Rev. Lett.* **71**, 1994 (1993).
- [6] V. E. Nefedova, M. F. Ciappina, O. Finke, M. Albrecht, J. Vábek, M. Kozlová, N. Suárez, E. Pisanty, M. Lewenstein, and J. Nejd, *Phys. Rev. A* **98**, 033414 (2018).
- [7] S. Roscam Abbing, F. Campi, F. S. Sajjadian, N. Lin, P. Smorenburg, and P. M. Kraus, *Phys. Rev. Appl.* **13**, 054029 (2020).
- [8] Z. Chang, *Fundamentals of Attosecond Optics* (Taylor & Francis, Boca Raton, Florida, 2011).
- [9] M. Krüger, D. Azoury, B. D. Bruner, and N. Dudovich, *Appl. Sci.* **9**, 378 (2019).
- [10] J. Peatross and D. D. Meyerhofer, *Phys. Rev. A* **52**, 3976 (1995).
- [11] M. Bellini, C. Lyngå, A. Tozzi, M. B. Gaarde, T. W. Hänsch, A. L'Huillier, and C.-G. Wahlström, *Phys. Rev. Lett.* **81**, 297 (1998).
- [12] H. Merdji, M. Kovačev, W. Boutu, P. Salières, F. Vernay, and B. Carré, *Phys. Rev. A* **74**, 043804 (2006).
- [13] E. Brunetti, R. Issac, and D. A. Jaroszynski, *Phys. Rev. A* **77**, 023422 (2008).
- [14] C. M. Kim and C. H. Nam, *J. Phys. B: At. Mol. Opt. Phys.* **39**, 3199 (2006).
- [15] T. Augustine, P. Salières, A. S. Wyatt, A. Monmayrant, I. A. Walmsley, E. Cormier, A. Zaïr, M. Holler, A. Guandalini, F. Schapper, J. Biegert, L. Gallmann, and U. Keller, *Phys. Rev. A* **80**, 033817 (2009).
- [16] W. Cao, G. Laurent, C. Jin, H. Li, Z. Wang, C. D. Lin, I. Ben-Itzhak, and C. L. Cocke, *J. Phys. B: At. Mol. Opt. Phys.* **45**, 074013 (2012).
- [17] P. Lan, M. Ruhmann, L. He, C. Zhai, F. Wang, X. Zhu, Q. Zhang, Y. Zhou, M. Li, M. Lein, and P. Lu, *Phys. Rev. Lett.* **119**, 033201 (2017).
- [18] F. Calegari, D. Ayuso, A. Trabattoni, L. Belshaw, S. D. Camillis, S. Anumula, F. Frassetto, L. Poletto, A. Palacios, P. Decleva, J. B. Greenwood, F. Martín, and M. Nisoli, *Science* **346**, 336 (2014).
- [19] D. Rupp, N. Monserud, B. Langbehn, M. Sauppe, J. Zimmermann, Y. Ovcharenko, T. Möller, F. Frassetto, L. Poletto, A. Trabattoni, F. Calegari, M. Nisoli, K. Sander, C. Peltz, M. J. Vrakking, T. Fennel, and A. Rouzée, *Nat. Commun.* **8**, 493 (2017).
- [20] T. Kita, T. Harada, N. Nakano, and H. Kuroda, *Appl. Opt.* **22**, 512 (1983).
- [21] M. Kumar, H. Singhal, J. A. Chakera, and P. A. Naik, *Appl. Spectrosc.* **72**, 1416 (2018).
- [22] T. Kanai, X. Zhou, T. Sekikawa, S. Watanabe, and T. Togashi, *Opt. Lett.* **28**, 1484 (2003).
- [23] J. Jiang, P. Wei, Z. Zeng, J. Miao, Y. Zheng, X. Ge, C. Li, R. Li, and Z. Xu, *Opt. Express* **22**, 15975 (2014).
- [24] P. Ye, X. He, H. Teng, M. Zhan, S. Zhong, W. Zhang, L. Wang, and Z. Wei, *Phys. Rev. Lett.* **113**, 073601 (2014).
- [25] Y. Pan, F. Guo, C. Jin, Y. Yang, and D. Ding, *Phys. Rev. A* **99**, 033411 (2019).
- [26] C. Corsi, A. Pirri, E. Sali, A. Tortora, and M. Bellini, *Phys. Rev. Lett.* **97**, 023901 (2006).
- [27] F. Schapper, M. Holler, T. Auguste, A. Zaïr, M. Weger, P. Salières, L. Gallmann, and U. Keller, *Opt. Express* **18**, 2987 (2010).
- [28] N. B. Delone and V. P. Krainov, *Phys. Usp.* **41**, 469 (1998).
- [29] S. C. Rae, *Opt. Commun.* **97**, 25 (1993).
- [30] F. Druon, G. Chériaux, J. Faure, J. Nees, M. Nantel, A. Maksimchuk, G. Mourou, J. C. Chanteloup, and G. Vdovin, *Opt. Lett.* **23**, 1043 (1998).
- [31] J. Rothhardt, G. K. Tadesse, W. Eschen, and J. Limpert, *J. Opt.* **20**, 113001 (2018).
- [32] G. Genoud, O. Guilbaud, E. Mengotti, S.-G. Pettersson, E. Georgiadou, E. Pourtal, C.-G. Wahlström, and A. L'Huillier, *Appl. Phys. B* **90**, 533 (2008).
- [33] H. Kim, P. Baksh, M. Odstreil, M. Miszczak, J. G. Frey, L. Juschkina, and W. S. Brocklesby, *Appl. Phys. Express* **9**, 076701 (2016).
- [34] J.-F. Hergott, P. Salières, H. Merdji, L. Le Déroff, B. Carré, T. Auguste, P. Monot, P. D'oliveira, D. Descamps, J. Norin, C. Lyngå, A. L'Huillier, C.-G. Wahlström, M. Bellini, and S. Huller, *Laser Part. Beams* **19**, 35 (2001).

- [35] M. Born, L. N. L. M. Born, E. Wolf, M. A. Born, and A. B. Bhatia, *Principles of Optics: Electromagnetic Theory of Propagation, Interference and Diffraction of Light* (Cambridge University Press, Cambridge, UK, 1999).
- [36] T. Ditmire, J. W. G. Tisch, E. T. Gumbrell, R. A. Smith, D. D. Meyerhofer, and M. H. R. Hutchinson, *Appl. Phys. B* **65**, 313 (1997).
- [37] L. Le Déroff, P. Salières, B. Carré, D. Joyeux, and D. Phalippou, *Phys. Rev. A* **61**, 043802 (2000).
- [38] K. D. Moeller, *Optics: Learning by Computing, with Examples Using Maple, MathCad®, Matlab®, Mathematica®, and Maple®*, 2nd ed. (Springer-Verlag, New York, 2007).
- [39] H. Dachraoui, T. Auguste, A. Helmstedt, P. Bartz, M. Michelswirth, N. Mueller, W. Pfeiffer, P. Salières, and U. Heinzmann, *J. Phys. B: At. Mol. Opt. Phys.* **42**, 175402 (2009).
- [40] F. Xie, Y. Li, X. Wang, Y. Wang, G. Lei, and K. Xing, *Int. J. Therm. Sci.* **124**, 131 (2018).
- [41] M. Kumar, H. Singhal, J. A. Chakera, P. A. Naik, R. A. Khan, and P. D. Gupta, *J. Appl. Phys.* **114**, 033112 (2013).
- [42] L. He, P. Lan, Q. Zhang, C. Zhai, F. Wang, W. Shi, and P. Lu, *Phys. Rev. A* **92**, 043403 (2015).